Particle & Particle Systems Characterization

www.particle-journal.com

A Facile Strategy to Synthesize Cobalt-Based Self-Supported Material for Electrocatalytic Water Splitting

Li Gu, Han Zhu, DanNi Yu, SongGe Zhang, Jiawei Chen, Juan Wang, Meng Wan, Ming Zhang, and MingLiang Du**

Designing and developing active, robust, and noble-metal-free catalysts with superior stability for electrocatalytic water splitting is of critical importance but remains a grand challenge. Here, a facile strategy is provided to synthesize a series of Co-based self-supported electrode materials by combining electrospinning and chemical vapor deposition (CVD) technologies. The Co, Co_3O_4, Co_9S_8 nanoparticles (NPs) are formed in situ simultaneously with the formation of carbon nanofibers (CNFs) during the CVD process, respectively. The Co-based NPs are uniformly distributed through the CNFs and they can be directly used as the electrode materials for hydrogen evolution reaction (HER) in acid and oxygen evolution reaction (OER) in alkaline. The Co_9S_8/CNFs membrane exhibits the best HER activity with overpotential of 165 mV at $j = 10$ mA cm^{-2} and Tafel slope of 83 mV dec^{-1} and OER activity with overpotential of 230 mV at $j = 10$ mA cm^{-2} and Tafel slope of 72 mV dec^{-1}. The onion-like graphitic layers formed around the NPs not only improve the electrical conductivity of the electrode but also prevent the separation of the NPs from the carbon matrix as well as the aggregation.

1. Introduction

The increasing environmental issues and energy demands caused by fossil fuel combustion have stimulated tremendous efforts in exploring clean energy sources.[1–3] As a green energy with high energy density, hydrogen (H_2) is considered to be a promising alternative to replace fossil fuels.[4,5] Electrocatalytic water splitting including two half-reactions: hydrogen evolution reaction (HER) and oxygen evolution reaction (OER) is an efficient reliable technology to achieve mass production of high-purity hydrogen with low cost and zero emission.[6–8] The slow kinetics of water splitting and the high overpotentials necessitate high-performance catalysts to decrease the electrolysis cell voltage and power consumption.[9,10] However, the platinum- and iridium-based catalysts are still the most active HER and OER catalysts and the low reserves and the high cost limits its application in large-scale water splitting.[11,12]

Designing and developing active, robust, and noble-metal-free catalysts with superior stability is of critical importance but remains a grand challenge.[13–15] Recently, transition metal compounds including chalcogenides, oxides, nitrides, and carbides exhibit high stability, corrosion resistance, and low cost and thus have been widely used in electrocatalysis,[16,17] lithium-air batteries,[18,19] and solar cells.[20,21] In view of thermodynamic convenience, transition metal chalcogenides such as MoS_2,[22] WS_2,[23] and CoS[24] have shown promising HER catalytic performance in acidic electrolytes, while many nonprecious OER catalysts based on transition metal oxides/hydroxides such as Fe_2O_3,[25] Co_3O_4/C,[26] MnO_2,[27] NiFe LDH,[28] etc. The current prevailing strategies often result in incompatible integration of the two catalysts or mediocre performance for complete water splitting. It is therefore highly imperative to develop electrocatalysts for both HER and OER to achieve efficient water splitting.

Recently, great effort has been devoted to developing efficient nanostructured for water splitting.[29,30] In order to enhance the electrocatalytic efficiency, the nanoscyrtal catalysts usually supported on carbon matrix, which also plays a critical role in catalysis. The large variety of carbon nanostructures such as carbon nanotubes, graphene, and porous carbon, have shown promising performance as substrates for many electrocatalysts.[31–33] The carbon nanostructures can protect the nanocrystal catalysts from acid corrosion and enhance the stability in acid. In addition, the heteroatoms, especially N or S doping in carbon nanostructures, will further modify the electronic structure of the catalysts and optimize the adsorption energy of the key intermediates on the surface.[34–36]

Here, we provide a facile strategy to synthesize a series of Co-based self-supported electrode materials by combining electrospinning and chemical vapor deposition (CVD) technologies. The Co salt were first dissolved in polyacrilonitrile/*N*,*N*-dimethylformamide (PAN/DMF) solution and the mixture were electrospun into Co salt/PAN nanofiber membrane. The Co,

L. Gu, Dr. H. Zhu, D. N. Yu, S. G. Zhang, J. W. Chen, J. Wang, M. Wan, Dr. M. Zhang, Prof. M. L. Du
College of Materials and Textiles
Key Laboratory of Advanced Textile Materials and Manufacturing Technology of the Ministry of Education
Zhejiang Sci-Tech University
Hangzhou 310018, P. R. China
E-mail: zhuhanfj@163.com; du@jiangnan.edu.cn

Dr. H. Zhu, Prof. M. L. Du
Key Laboratory of Synthetic and Biological Colloids
Ministry of Education
School of Chemical and Material Engineering
Jiangnan University
Wuxi 214122, P. R. China

The ORCID identification number(s) for the author(s) of this article can be found under https://doi.org/10.1002/ppsc.201700189.

DOI: 10.1002/ppsc.201700189

Co_3O_4, Co_9S_8 NPs were formed in situ simultaneously with the formation of CNF during the CVD process, respectively. The preparation of Co-based/CNF composites is regarded as a one-step process, which allows easy quality control, good reproducibility, and cost-effectiveness. The Co-based NPs were uniformly distributed through the CNFs and they can be directly used as the electrode materials for HER in acid and OER in alkaline. The Co_9S_8/CNFs membrane exhibit the best HER activity with overpotential of 165 mV at j = 10 mA cm^{-2} and Tafel slope of 83 mV dec^{-1} and OER activity with overpotential of 230 mV at j = 10 mA cm^{-2} and Tafel slope of 72 mV dec^{-1}. The superior electrocatalytic activity is attributed to the uniform dispersion of active NPs in the CNF matrix. The onion-like graphitic layers formed around the NPs not only improve the electrical conductivity of the electrode but also prevent the separation of the NPs from the carbon matrix as well as the aggregation. This approach suggests a good potential applications of these new nanocrystal/CNF hybrid in energy related fields.

2. Results and Discussion

Figure 1 shows the typical transmission electron microscopy (TEM) and scanning electron microscopy (SEM) images of the synthesized Co-based CNFs membrane. As shown in Figure 1a,d, large amounts of the quasi spherically shaped Co nanoparticles (NPs) uniformly distributed in the CNFs matrix. The further magnified TEM image of the single nanofiber in Figure 1d,g demonstrates that the Co NPs are covered by several carbon layers, and the carbon layers could protect the catalysts from degradation during the electrocatalysis operation. Compared with the smooth surfaces of neat CNFs, the Co/CNFs membrane exhibits porous structures and there are larger amounts of the onion-like pores that can be observed, which are beneficial for the access of the electrolyte onto the surfaces of the active sites. The diameter of CNF ranges from 200 to 500 nm and the length lies in the scale of tens of micrometers. The size of the Co NPs ranged from 5 to 30 nm and the good distribution of NPs in CNF is attributed to the in situ formation of Co NPs and CNF during the high-temperature thermal treatment, where the Co NPs were firmly locked within the CNF matrix.

Figure 1b,e displays the morphologies of the Co_9S_8/CNFs membrane. After the sulfuration, the Co_9S_8 NPs become relatively larger and the size lies in the range from 10 to 50 nm. Accordingly, the Co_9S_8/CNFs exhibit numerous relative larger pores, when compared with the Co/CNFs. For the Co_3O_4/CNFs membrane, the porous structure still remains and the onion-like pores become larger because of the increased Co_3O_4 size ranged from 10 to 40 nm. The surfaces of the Co_3O_4 NPs are also covered by several carbon layers. After the sulfuration and oxidation process, the Co_9S_8 and Co_3O_4 NPs are still uniformly distributed throughout the CNFs without significant aggregation. The onion-like graphitic layers not only improve the electrical conductivity of the nanocrystals but also prevent the degradation of the nanocrystals from the electrolyte during the electrocatalysis.

Scanning transmission electron microscopy-high-angle annular dark-field imaging (STEM-HAADF) (**Figure 2**) and STEM-energy-dispersive X-ray spectroscopy (STEM-EDX) characterizations provide more information about the as-prepared Co-based CNF membrane. As shown in Figure 2a,b, the energy dispersive spectroscopy STEM-EDX element mapping demonstrate carbon, nitrogen, cobalt, and oxygen elements. The carbon and nitrogen are ascribed to the CNF, indicating the N-doped carbon materials. The cobalt and oxygen match well, suggesting the successfully formation of the Co_3O_4 in CNF. High-resolution TEM (HRTEM, Figure 2c) images display the

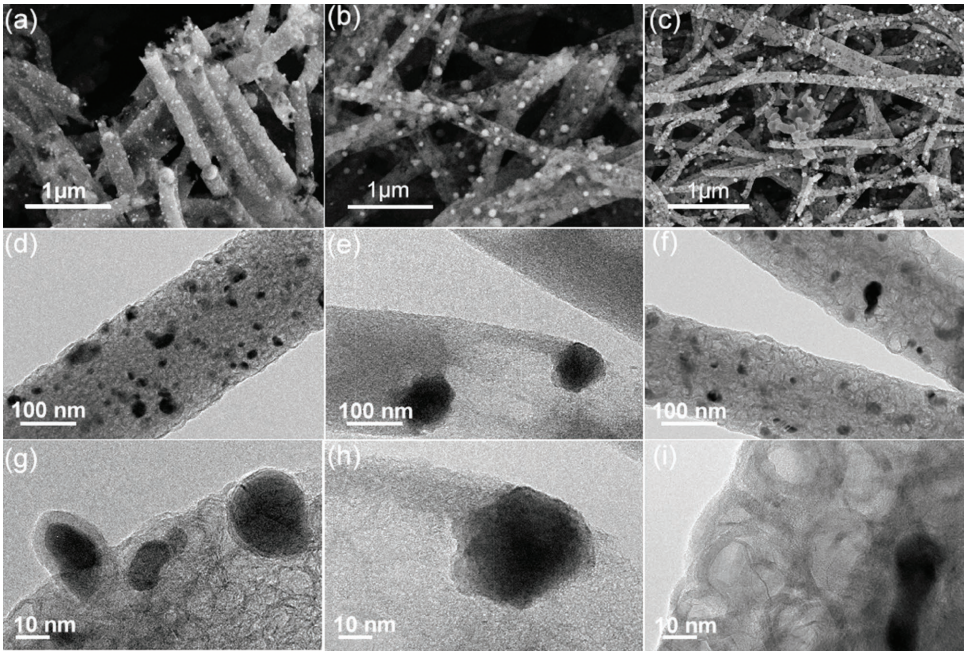

Figure 1. FE-SEM and TEM images of the a,d,g) Co/CNFs, b,e,h) Co_9S_8/CNFs, and c,f,i) Co_3O_4/CNFs.

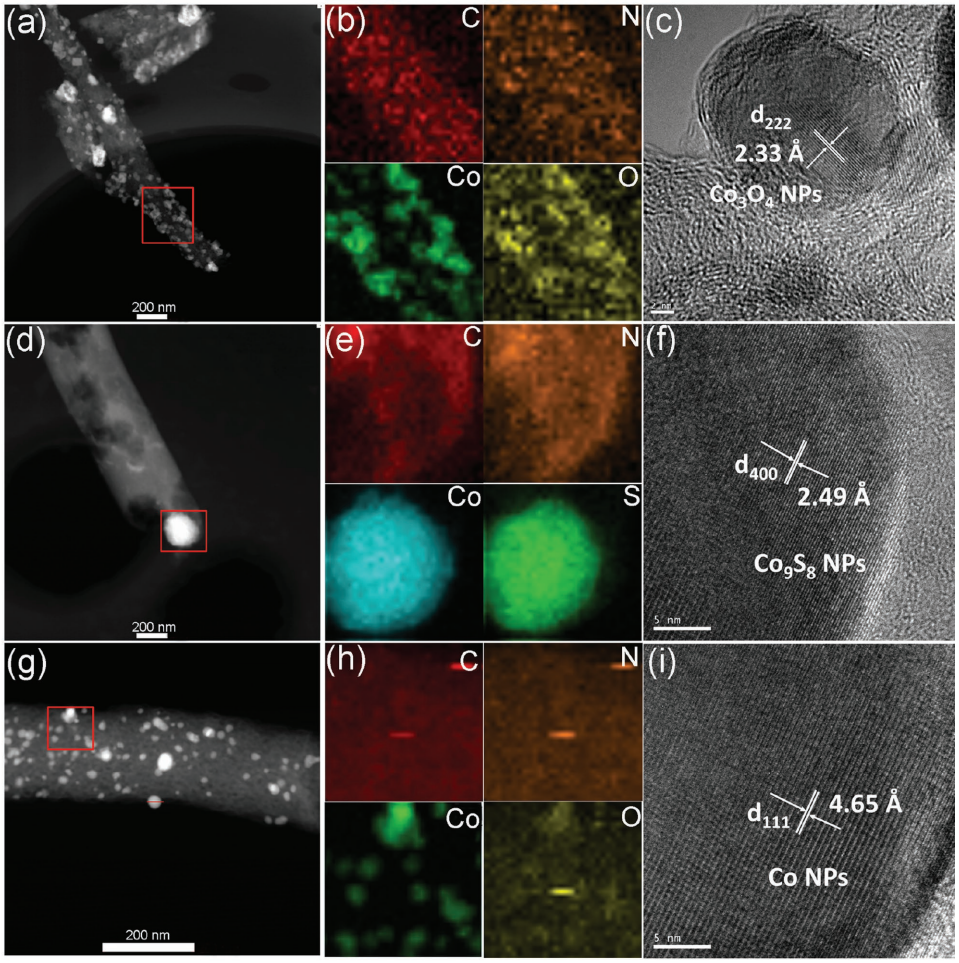

Figure 2. HAADF-STEM, STEM-EDX mapping, and HRTEM images of the a–c) Co_3O_4/CNFs, d–f) Co_9S_8/CNFs, and g–i) Co/CNFs.

well-resolved lattice fringes with interplanar spacing of 0.23 nm, corresponding to the Co_3O_4 (222) plane of face-centered cubic (fcc) phase. As shown in Figure 2d,e, the STEM-HAADF and STEM-EDX element mapping images both verified the successful synthesis of the Co_9S_8 NPs. The carbon and nitrogen are ascribed to the N-doped CNFs and the cobalt and sulfur are attributed to the Co_9S_8 NPs. HRTEM image (Figure 2f) of a single Co_9S_8 NP displays well-resolved lattice fringes with interplanar spacing of 2.49 Å, corresponding to the Co_9S_8 (400) plane of face-centered cubic (fcc) phase. As shown in Figure 2g–i, the Co/CNF also exhibits four elements including carbon, nitrogen, cobalt, and oxygen. The carbon, nitrogen, and oxygen are ascribed to the N-doped CNF matrix, indicating that the Co NPs are metallic state. HRTEM shows the (111) planes of the Co NPs with well-resolved interplanar spacing of 4.65 Å.

Figure 3a shows the X-ray diffraction (XRD) pattern for the Co/CNFs, Co_3O_4/CNFs, and Co_9S_8/CNFs, respectively. The Co/CNFs exhibit two sharp peaks located at 44.1° and 51.6°, corresponding to the (111) and (220) planes of Co NPs.[37,38] The broad peak centered at 23.0° is ascribed to the amorphous carbon while the sharp peak located at 26.0° corresponds to the graphite carbon caused by the catalytic effect of Co NPs. For the Co_3O_4/CNFs, the major peaks were located at 37.6°, 44.2°, 64.7°, and 77.7°, corresponding to the (222), (400), (440), and (533) reflections of Co_3O_4 (JCPDS No. 078-1970), respectively.[39,40] The Co_9S_8/CNFs membrane displays two peaks located at 29.8° and 51.8°, and all of the diffraction peaks can be readily indexed to the cubic Co_9S_8 phase (JCPDS no. 19-0364, space group: *Fm3m*).[41,42] XRD results indicate the successful formation of the Co/CNFs, Co_3O_4/CNFs, and Co_9S_8/CNFs membrane.

X-ray photoelectron spectroscopy (XPS) was employed to investigate the chemical states and bonding states. Figure 3b displays the Co 2p XPS spectra of the Co/CNFs, and the deconvoluted Co 2p spectra show four binding energies (BEs) at 778.3, 781.8, 793.3, and 799.4 eV, respectively. The BEs at 778.3 and 793.3 eV correspond to the Co $2p_{3/2}$ and Co $2p_{1/2}$ and the Co $2p_{3/2}$–$2p_{1/2}$ energy separation is ≈15.0 eV. The Co 2p BE at 778.3 eV belongs to the metallic form of Co NPs, further confirming the formation of Co NPs in CNFs.[43,44] For the Co_3O_4/CNFs membrane, as shown in Figure 3c, the Co_3O_4 exhibits two chemical states with BEs at 781.1 and 783.3 eV, corresponding to the Co (II) and Co (III) states.[45,46] The BEs of Co 2p located at 781.1 and 796.8 eV are ascribed to the Co $2p_{3/2}$ and Co $2p_{1/2}$ and the Co $2p_{3/2}$–$2p_{1/2}$ energy separation is ≈15.7 eV. The absence of the prominent shake up satellite peaks in the Co 2p

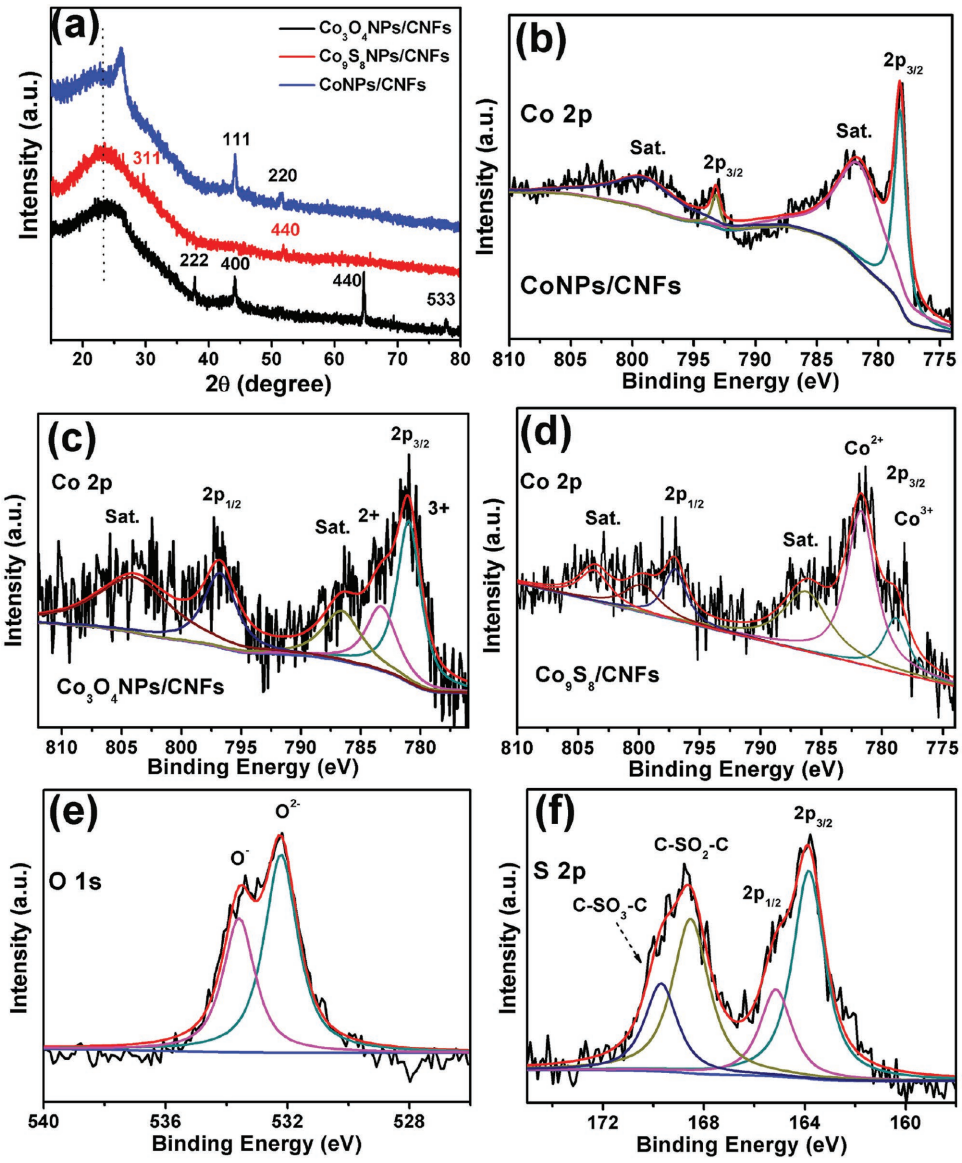

Figure 3. a) XRD patterns of the Co_3O_4/CNFs, Co_9S_8/CNFs, and Co/CNFs. Co 2p XPS spectra of the b) Co_3O_4/CNFs, c) Co_9S_8/CNFs, and d) Co/CNFs. e) O 1s XPS spectra of the Co_3O_4/CNFs. f) S 2p XPS spectra of the Co_9S_8/CNFs.

spectra indeed suggests the presence of a Co_3O_4 phase.[45,46] The O 1s XPS spectra for the Co_3O_4/CNFs (Figure 3e) further reveal the two oxygen states of O^{2-} at 532.2 eV and O^- at 533.5 eV.[45,46] The O^{2-} peaks were related to the oxygen in the Co_3O_4, and the peaks of O^{2-} represented chemisorbed oxygen species. The XPS results are accordingly with the reported Co_3O_4 crystals.

As shown in Figure 3d, the peaks at 778.8, 781.8 and 797.0, 799.8 eV correspond to the BEs of Co $2p_{3/2}$ and Co $2p_{1/2}$ of Co (II) and Co (III) states in Co_9S_8, respectively.[47,48] Another two weak peaks at 786.3 and 803.7 eV can be the shake-up satellite peaks above the main peaks, suggesting the presence of Co(II).[47,48] In addition, as shown in Figure 3f, the S 2p XPS spectra exhibit two peaks at 163.8 and 165.2 eV that are ascribed to the S $2p_{3/2}$ and S $2p_{1/2}$ derived from the sulfur atoms in Co_9S_8. The existence of different binding states for S at 168.5 ($C–SO_2–C$) and 169.7 eV ($C–SO_3–C$) indicates that the S atoms have also been successfully incorporated into the carbon matrix (**Figure 4**c).[49,50] XPS results can further demonstrate the differences in metallic Co, Co_3O_4, and Co_9S_8 NPs.

The electrocatalytic performance of the as-prepared Co_9S_8/CNFs, Co/CNFs, Co_3O_4/CNFs membrane for HER and OER has been investigated in 0.5 M H_2SO_4 and 1 M KOH solution using a typical three-electrode setup, respectively. All the membranes were cut into 1 × 1 cm^2 squares and directly used as the working electrode. A graphite rod and a saturated calomel electrode were used as the counter and reference electrodes, respectively. As shown in Figure 4a,b, the Co/CNFs exhibit an overpotential of 225 mV at current density j = 10 mA cm^{-2} and a Tafel slope of 121 mV dec^{-1}. The Co_9S_8/CNFs electrode obtained an overpotential of 165 mV at j = 10 mA cm^{-2}, which are better than that for Co_3O_4/CNFs (304 mV). The corresponding Tafel slopes for Co_9S_8/CNFs and Co_3O_4/CNFs are

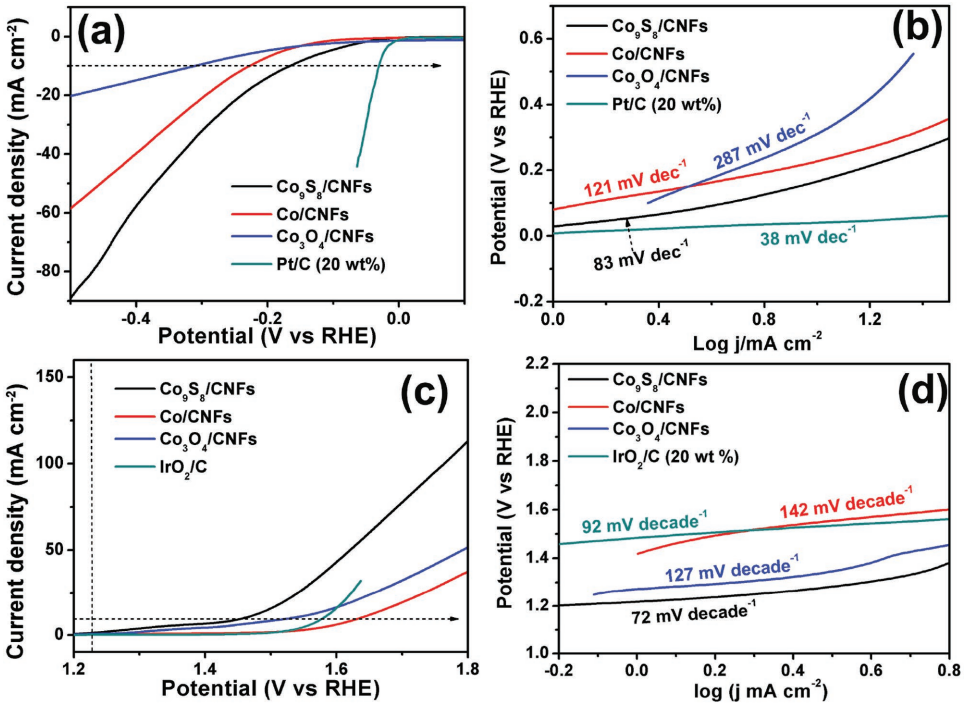

Figure 4. Electrocatalytic performance of the as-prepared self-supported nanomaterials for HER in acid and OER in alkane. a) The polarization curves of the Co_9S_8/CNFs, Co/CNFs, Co_3O_4/CNFs, and Pt/C electrocatalysts obtained in 0.5 M H_2SO_4 with a scan rate of 2 mV s^{-1}. b) The corresponding Tafel slopes of the Co_9S_8/CNFs, Co/CNFs, Co_3O_4/CNFs, and Pt/C electrocatalysts. c) The polarization curves of the Co_9S_8/CNFs, Co/CNFs, Co_3O_4/CNFs, and IrO_2/C electrocatalysts obtained in 1 M KOH with a scan rate of 2 mV s^{-1}. d) The corresponding Tafel slopes of the Co_9S_8/CNFs, Co/CNFs, Co_3O_4/CNFs, and IrO_2/C electrocatalysts.

83 and 287 mV dec^{-1}, respectively. Obviously, the Pt/C catalyst obtained the lowest overpotential (28 mV at j = 10 mA cm^{-2}) and the smallest Tafel slope (38 mV dec^{-1}) along with a prominent current density.

Catalytic activities for OER are shown in Figure 4c,d, including linear sweep voltammetry (LSV) driven to higher values than water oxidation standard potential, 1.23 V versus RHE and the corresponding Tafel plots. The polarization curves recorded with Co_9S_8/CNFs, Co_3O_4/CNFs, and Co/CNFs electrodes display the relative lower overpotentials of 230, 300, and 402 mV at j = 10 mA cm^{-2}, when compared with the IrO_2/C catalysts (350 mV). Obviously, the Co_9S_8/CNFs display the state-of-the-art overpotential values with an excellent catalytic activity. The corresponding Tafel slopes of the electrodes are 72, 127, and 142 mV dec^{-1}, respectively, which are lower than the IrO_2/C (92 mV dec^{-1}). The higher sensitivity of the electric current response to the applied potential for the Co-based electrodes indicates that these electrodes have much more favorable kinetics. The Co_9S_8/CNFs exhibited a Tafel value of 72 mV dec^{-1}, demonstrating the faster reaction kinetics and higher sensitivity to overpotential of the electrocatalytic activity of this electrode.

Stability is another important criterion for the electrode materials. As shown in **Figure 5**a, the time-dependent current density at η = 300 mV indicates that after the continuous HER operation for 10 h, the Co_9S_8/CNFs electrode still retains a current density of 72%, which is larger than the benchmark Pt/C catalysts (55%). In addition, for the OER continuous operation investigation, the Co_9S_8/CNFs electrode obtains a current density of 84% while the benchmark Pt/C catalysts retain a current density of 57%. In addition, the polarization curves for Co_9S_8/CNFs before and after 1000 cycles, as shown in Figure S1 (Supporting Information), also exhibit small degradation in current density, further confirming the superior stability of Co_9S_8/CNFs under HER and OER operations. The field emission SEM (FE-SEM) and TEM images of the Co_9S_8/CNFs membrane after continuous OER process (Figure S2, Supporting Information) indicated that the Co_9S_8 NPs were still densely immobilized on the CNFs, suggesting no dissolving of the Co_9S_8 NPs.

In order to further investigate the kinetics of the electrode in the acid solution during the HER process, the electrochemical impedance spectroscopy (EIS) measurements were performed. As shown in Figure 5c, the Nyquist plots of the three electrodes obtained at η = 300 mV indicate that the reaction is kinetically controlled. There is only one semicircle in the plot, demonstrating that the equivalent circuit is characterized by only one time constant. The solution resistance (R_s) for all electrodes is about 6 Ω. The charge transfer resistances (R_{ct}) among the Co_9S_8/CNFs, Co/CNFs, and Co_3O_4/CNFs are about 72.0, 93.3, and 153.9 Ω, respectively. It is well-known that the R_{ct} is strongly associated with the kinetics of the HER, and therefore, the lower R_{ct} of Co_9S_8/CNFs suggests a higher electrocatalytic activity toward HER. The host CNF can enhance the conductivity of the support catalyst and decrease the charge transfer resistance. The superior electrocatalytic activities are attributed to the uniform dispersion of active NPs in the CNF matrix. The onion-like graphitic layers formed around the NPs not only

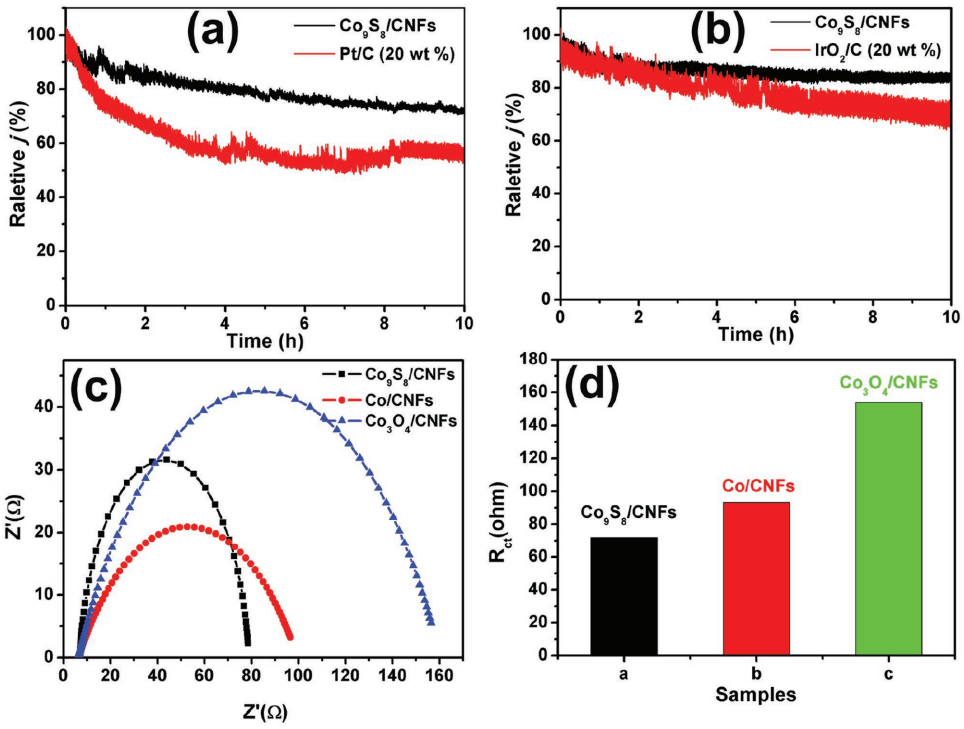

Figure 5. a) The relative time-dependent current density of the Co_9S_8/CNFs and Pt/C electrodes at a constant voltage of –0.4 V versus RHE. b) The relative time-dependent current density of the Co_9S_8/CNFs and Pt/C electrodes at a constant voltage of 1.45 V versus RHE. c) The Nyquist plots of the Co_9S_8/CNFs, Co/CNFs, and Co_3O_4/CNFs electrocatalysts performed at –0.3 V versus RHE. d) The calculated R_{ct} of the Co_9S_8/CNFs, Co/CNFs, and Co_3O_4/CNFs.

improve the electrical conductivity of the electrode but also prevent the separation of the NPs from the carbon matrix as well as the aggregation. This approach suggests a good potential of this new nanocrystal/CNF hybrid in energy related applications.

3. Conclusions

Here, we provide a facile strategy to synthesize a series of Co-based self-supported electrode materials by combining electrospinning and CVD technologies. The Co, Co_3O_4, Co_9S_8 NPs were formed in situ simultaneously with the formation of CNF during the CVD process, respectively. The Co-based NPs were uniformly distributed through the CNFs and they can be directly used as the electrode materials for HER in acid and OER in alkaline. The Co_9S_8/CNFs membrane exhibits the best HER activity with overpotential of 165 mV at $j = 10$ mA cm^{-2} and Tafel slope of 83 mV dec^{-1} and OER activity with overpotential of 230 mV at $j = 10$ mA cm^{-2} and Tafel slope of 72 mV dec^{-1}. This approach suggests a good potential of these new nanocrystal/CNF hybrid in energy related applications.

4. Experimental Section

Preparation of the Co Precursor/PAN Electrospun Nanofibers Membrane: In a typical approach, 1.5 g PAN were first dissolved in 22 mL DMF solvent to get a transparent solution. Then, 0.5 g $Co(NO_3)_2$ were dissolved in PAN/DMF solution for 5 h under magnetic stirring to get a homogeneous mixture. The mixture was transferred to a 10 mL plastic syringe with a 20-gauge blunt tip needle. For the electrospinning process, a high voltage of 18 kV and a flow rate of 0.6 mL h^{-1} were applied, with a distance of 15 cm between the needle and rotating grounded collector.

Synthesis and Preparation of the Co-Based (Co, Co_3O_4, and Co_9S_8) CNF Membrane: The as-prepared Co/PAN precursor membrane was placed in a home-built chemical CVD furnace system. To prepare the Co/CNFs membrane, the Co/PAN precursor membrane was first preoxidized at 280 °C for 3 h in air and then carbonized at 1000 °C for 6 h in Ar atmosphere with a heating rate of 5 °C min^{-1}. To prepare the Co_3O_4/CNFs, the Co/PAN precursor membrane was first preoxidized at 280 °C for 3 h in air and then oxidized at 500 °C for 1 h. After that the membrane were carbonized at 1000 °C for 6 h in Ar atmosphere with a heating rate of 5 °C min^{-1}. For the preparation of Co_9S_8/CNFs, the Co/PAN precursor membrane was first preoxidized at 280 °C for 3 h in air and then stabilized under sulfuration at 500 °C for 1 h. After that the membrane was carbonized at 1000 °C for 6 h in Ar atmosphere with a heating rate of 5 °C min^{-1}.

Synthesis and Preparation of the Co-Based (Co, Co_3O_4, and Co_9S_8) CNF Membrane—Instrument: The morphology of the prepared samples was observed on a JSM-6700F FE-SEM (JEOL, Japan) at an acceleration voltage of 3 kV. Transmission electron microscopy and scanning transmission electron microscopy were performed using a transmission electron microscope (Tecnai G2 F30S-Twin, Philips-FEI) at an acceleration voltage of 300 kV. X-ray diffraction patterns of the hybrid membrane were obtained on a diffractometer (Bruker AXS D8) using Cu Kα radiation ($\lambda = 1.5406$ Å) with a 2θ scan from 5° to 80° at a step of 0.02. X-ray photoelectron spectra of the samples were recorded using an X-ray photoelectron spectrometer (Kratos Axis Ultra DLD) with an aluminum (mono) Kα source (1486.6 eV).

Synthesis and Preparation of the Co-Based (Co, Co_3O_4, and Co_9S_8) CNF Membrane—Electrochemical Measurements: All electrochemical tests were performed at room temperature in a standard three-electrode system controlled by an Autolab potentiostat/galvanostat (Model PGSTAT302N) workstation. A carbon rod and a saturated calomel

electrode (SCE) were used as the counter and reference electrode, respectively. In all measurements, the potentials were referenced to an RHE by adding a value of (0.244 + 0.059 pH) V for SCE. The Ohmic potential drop (iR) losses that arise from the solution resistance were all corrected. Tafel plots of the overpotential versus log (current density) are recorded with the linear portions at low overpotential fitted to the Tafel equation ($\eta = a + b \log j$, where η is the overpotential, j is the cathodic current density, and b is the Tafel slope). Commercial Pt/C (Johnson Matthey, 20 wt%) was cast on a glassy carbon disk of 3 mm diameter with a catalyst loading of 220 mg cm^{-2}. The as-prepared membrane was cut into 1 × 1 cm^{-2} squares and fixed with a Teflon electrode clamp to be used directly as the working electrode. The HER and OER performance of the electrodes was measured in a 0.5 M H_2SO_4 and 1 M KOH electrolyte, respectively. The electrolyte was purged with nitrogen for at least 30 min before each test, and a nitrogen environment was maintained at all times to eliminate dissolved oxygen in the solution. The performance of the catalysts was recorded by LSV at a scan rate of 2 mV s^{-1}. EIS was carried out at –0.3 V versus RHE over a frequency range from 10^{-2} to 10^6 Hz.

Supporting Information

Supporting Information is available from the Wiley Online Library or from the author.

Acknowledgements

This study was supported by the National Natural Science Foundation of China (NSFC) (Grant nos. 51373154 and 51573166), the MOE & SAFEA, the (111) Project (B13025) and the Foundation of Key Laboratory of Advanced Textile Materials and Manufacturing Technology (Grant no. 2016QN07).

Conflict of Interest

The authors declare no conflict of interest.

Keywords

cobalt-based electrocatalysts, electrospinning, hydrogen energy, transition metal compounds, water splitting

Received: May 29, 2017
Revised: June 22, 2017
Published online: July 25, 2017

[1] J. Duan, S. Chen, A. Vasileff, S. Qiao, *ACS Nano* **2016**, *10*, 8738.
[2] X. Li, W. Liu, M. Zhang, Y. Zhong, Z. Weng, Y. Mi, Y. Zhou, M. Li, J. Cha, Z. Tang, H. Jiang, X. Li, H. Wang, *Nano Lett.* **2017**, *17*, 2057.
[3] X. Deng, H. Tiiysiiz, *ACS Catal.* **2014**, *4*, 3701.
[4] R. K. Das, Y. Wang, S. Vasilyeva, E. Donnoghue, L. Pucher, G. Kamenov, H. Cheng, A. Ringzler, *ACS Nano* **2014**, *8*, 8447.
[5] H. Fei, Y. Yang, Z. Peng, G. Ruan, Q. Zhog, L. Li, E. Samuel, J. Tour, *ACS Appl. Mater. Interfaces* **2015**, *7*, 8083.
[6] B. Chen, N. Morlanés, E. Adogla, K. Takanabe, V. Rodionov, *ACS Catal.* **2016**, *6*, 4647.
[7] Y. Ling, Y. Li, *Part. Part. Syst. Charact.* **2014**, *31*, 1113.
[8] Y. Yang, H. Fei, G. Ruan, C. Xiang, J. Tour, *ACS Nano* **2014**, *8*, 9518.
[9] C. Rakousky, U. Reimer, K. Wippermann, S. Kuhri, M. Carmo, W. Lueke, D. Stolten, *J. Power Sources* **2017**, *342*, 38.
[10] H. Li, A. Inada, T. Fujigaya, H. Nakajima, K. Sasaki, K. Ito, *J. Power Sources* **2016**, *318*, 192.
[11] B. You, N. Jiang, M. Sheng, S. Gul, J. Yano, Y. Sun, *Chem. Mater.* **2015**, *27*, 7636.
[12] Y. Wang, C. Xie, D. Liu, X. Huang, J. Huo, S. Wang, *ACS Appl. Mater. Interfaces* **2016**, *8*, 18652.
[13] B. You, N. Jiang, M. Sheng, S. Gul, J. Yano, Y. Sun, *Chem. Mater.* **2015**, *27*, 7636.
[14] X. Han, W. M. Chen, X. Han, Y. Z. Tan, D. Sun, *J. Mater. Chem. A* **2016**, *4*, 13040.
[15] H. Zhu, M. Du, M. Zhang, M. Zou, T. Zhang, S. Wang, T. Yao, B. Guo, *Chem. Commun.* **2014**, *50*, 15435.
[16] Z. Wei, J. Wang, S. Mao, D. Su, H. Jin, Y. Wang, F. Xu, H. Li, Y. Wang, *ACS Catal.* **2015**, *5*, 4783.
[17] H. Zhu, J. Zhang, R. Yanzhang, M. Du, Q. Wang, G. Gao, J. Wu, G. Wu, M. Zhang, B. Liu, J. Yao, X. Zhang, *Adv. Mater.* **2015**, *27*, 4752.
[18] J. Xu, Z. Wang, W. Yu, D. Sun, Q. Zhang, C. H. Tung, W. Wang, *ChemSusChem* **2016**, *9*, 1146.
[19] H. Jung, Y. Jeong, J. Park, Y. Sun, B. Scrosati, Y. Lee, *ACS Nano* **2013**, *7*, 3532.
[20] B. Qiu, Q. Zhu, M. Du, L. Fan, M. Xing, J. Zhang, *Angew. Chem.* **2017**, *129*, 2728.
[21] I. Liu, Y. Hou, C. Li, Y. Lee, *J. Mater. Chem. A* **2017**, *5*, 240.
[22] B. Liu, W. Zhao, Z. Ding, I. Verzhbitskiy, L. Li, J. Lu, J. Chen, G. Sda, K. Loh, *Adv. Mater.* **2016**, *28*, 6457.
[23] H. Hill, A. Rigosi, K. Rim, G. Flynn, T. Heinz, *Nano Lett.* **2016**, *16*, 4831.
[24] Y. Tang, F. Jing, Z. Xu, Y. Mai, D. Wu, *ACS Appl. Mater. Interfaces* **2017**, *9*, 12340.
[25] J. Yang, G. Zhu, Y. Liu, J. Xia, Z. Ji, X. Shen, S. Wu, *Adv. Funct. Mater.* **2016**, *26*, 4712.
[26] J. H. Xu, L. Y. Guo, H. F. Su, X. Gao, X. F. Wu, W. G. Wang, C. H. Tung, D. Sun, *Inorg. Chem.* **2017**, *56*, 1591.
[27] D. Wu, S. Xu, C. Zhang, Y. Zhu, D. Xiong, R. Huang, R. Qi, L. Wang, P. Chu, *J. Mater. Chem. A* **2016**, *4*, 11317.
[28] X. Li, X. Hao, Z. Wang, A. Abudula, *J. Power Sources* **2017**, *347*, 193.
[29] S. Cao, X. Yan, Z. Kang, Q. Liang, X. Liao, Y. Zhuang, *Nano Energy* **2016**, *24*, 25.
[30] J. Wang, H. Zhong, Z. Wang, F. Meng, X. Zhuang, *ACS Nano* **2016**, *10*, 2342.
[31] H. Ghanbarlou, S. Rowshanzamir, M. Parnian, F. Mehri, *Int. J. Hydrogen Energy* **2016**, *41*, 14665.
[32] P. Zamani, D. Higgins, F. Hassan, X. Fu, J. Choi, M. Hoque, G. Jiang, Z. Chen, *Nano Energy* **2016**, *26*, 267.
[33] C. Zhu, H. Li, S. Fu, D. Du, Y. Lin, *Chem. Soc. Rev.* **2016**, *45*, 517.
[34] Y. Zhu, C. Guo, Y. Zheng, S. Qiao, *Acc. Chem. Res.* **2017**, *50*, 915.
[35] K. Song, E. Cho, Y. Kang, *ACS Catal.* **2015**, *5*, 5116.
[36] H. Fei, Y. Yang, Z. Peng, G. Ruan, Q. Zhong, L. Li, E. Samuel, J. Tour, *ACS Appl. Mater. Interfaces* **2015**, *7*, 8083.
[37] H. Fei, Y. Yang, Z. Peng, G. Ruan, Q. Zhong, L. Li, E. L. G. Samuel, J. Tour, *ACS Appl. Mater. Interfaces* **2015**, *7*, 8083.
[38] B. Seo, Y. Sa, J. Woo, K. Kwon, J. Park, T. Shin, H. Jeong, S. Joo, *ACS Catal.* **2016**, *6*, 4347.
[39] S. Bartling, C. Yin, I. Barke, K. Oldenburg, H. Hartmann, V. Oeynhausen, M. Pohl, K. Houben, E. Tyo, S. Seifert, P. Lievens, K. Meiwes-Broer, S. Vajda, *ACS Nano* **2015**, *9*, 5984.
[40] P. Ganesan, M. Prabu, J. Sanetuntikul, J. Sanetuntikul, S. Shanmugam, *ACS Catal.* **2015**, *5*, 3625.
[41] B. Hu, Z. Jing, J. Fan, J. Fan, G. Yao, F. Jin, *Catal. Today* **2016**, *263*, 128.

[42] X. Cao, X. Zheng, J. Tian, C. Jin, K. Ke, R. Yang, *Electrochim. Acta* **2016**, *191*, 776.
[43] D. Merki, H. Vrubel, L. Rovelli, S. Fierro, X. Hu, *Chem. Sci.* **2012**, *3*, 2515.
[44] J. Liu, L. Jiang, B. Zhang, J. Jin, D. Su, S. Wang, G. Sun, *ACS Catal.* **2014**, *4*, 2998.
[45] C. Nethravathi, C. Rajamathi, M. Rajamathi, X. Wang, U. Gautam, D. Golberg, Y. Bando, *ACS Nano* **2014**, *8*, 2755.
[46] H. Zhu, L. Gu, D. Yu, Y. Sun, M. Wan, M. Zhang, L. Wang, L. Wang, W. Wu, J. Yao, M. Du, S. Guo, *Energy Environ. Sci.* **2017**, *10*, 321.
[47] S. Dou, L. Tao, J. Huo, S. Wang, L. Dai, *Energy Environ. Sci.* **2016**, *9*, 1320.
[48] J. Xu, Q. Wang, X. Wang, Q. Xiang, B. Liang, D. Chen, G. Shen, *ACS Nano* **2013**, *7*, 5453.
[49] A. Peters, Z. Li, O. Farha, J. Hupp, *ACS Nano* **2015**, *9*, 8484.
[50] M. Faber, R. Dziedzic, M. Lukowski, N. Kaiser, Q. Ding, S. Jin, *Chem. Soc. Rev.* **2014**, *136*, 10053.

